Surface elastic and molecular-anchoring properties of nematic liquid crystals confined to cylindrical cavities

G. P. Crawford, D. W. Allender, and J. W. Doane
Liquid Crystal Institute and ALCOM Center, Department of Physics, Kent State University, Kent, Ohio 44242-0001
(Received 10 February 1992)

The measurement of the saddle-splay surface elastic constant K_{24} in a nematic liquid crystal is reported based on two independent deuterium nuclear-magnetic-resonance (^{2}H-NMR) experiments. Fifty years after the pioneering work of Oseen and Zocher, these measurements were made from observations of nematic director-field configurations and a configuration transition discovered in submicrometer-sized cylindrical cavities of Nuclepore membranes under selected surface preparations and wall curvatures. The experimental difficulties in separating the effect of anchoring energy from surface elastic energy (inherent in small confining volumes) were overcome by a unique use of NMR and the ability to predict stable nematic structures with elastic theory. Direct comparison of calculated ^{2}H-NMR spectral patterns to experiment is very sensitive to the details of the stable nematic director-field configuration in cylindrical cavities. Small differences in the director configuration imposed by the curvature or elastic properties of the nematic liquid crystal are strongly reflected in the shape of the spectral pattern. Different nematic structures with preferred perpendicular anchoring conditions such as the escaped radial and planar polar show markedly different patterns. Theoretical analysis reveals that a planar-polar structure is preferred in cavities with a high degree of curvature or sufficiently weak anchoring conditions at the cavity boundary. The features of the planar-polar structure are described in terms of the dimensionless parameter RW_0/K, where R is the radius, W_0 is the molecular anchoring strength, and K is the bulk elastic constant in the one-constant approximation. At a sufficiently large radius or substantially strong anchoring conditions, the escaped-radial structure is favored and sensitive to the dimensionless surface parameter $\sigma = RW_0/K + K_{24}/K - 1$. The ^{2}H-NMR technique unambiguously distinguishes between these two stable nematic director-field configurations and is sensitive to the surface parameters σ and RW_0/K. Theoretical analysis also reveals that the relative magnitude of the bend (K_{33}) and splay (K_{11}) bulk elastic constants plays a vital role in determining the molecular anchoring angle at the cavity wall of the escaped-radial configuration. As K_{33}/K_{11} increases, the molecular anchoring angle is shown to deviate further from its preferred perpendicular orientation in the presence of finite molecular anchoring to alleviate the expensive bend deformation. Experimentally, point defects occur in the escaped-radial configuration where the direction of bend is changed, resulting is a series of alternating hyperbolic and radial defects. An analytical trial function is constructed that describes these defect structures in the region of interest.

PACS number(s): 64.70.Md, 61.30.By, 61.30.Jf, 68.10.Cr

I. INTRODUCTION

Despite the successful application of elastic theory to uniaxial liquid crystals pioneered by Oseen [1] and Zocher [2] more than 50 years ago, the importance of the surface elastic contributions has remained an open question because there have been no measurements of the associated surface elastic constant. The measurement of the surface elastic constants has been an experimental challenge for two basic reasons: The simultaneous presence of bulk elastic distortions and the effects of surface anchoring. A liquid-crystal material in its equilibrium configuration can exhibit three types of bulk deformations that are historically known as splay, twist, and bend. Each type of deformation is associated with a specific elastic constant K_{11}, K_{22}, and K_{33}, respectively, that describes the energy associated with the related deformations. The techniques for measuring the magnitude of bulk elastic constants are well established [3,4] and based on Fréedericksz-type experiments or empirically deriving a sample geometry that excites a particular deformation in a pure mode. The other two deformations do not contribute to the configuration. In principle three configurations are needed to determine K_{11}, K_{22}, and K_{33} accurately.

Unfortunately the surface elastic deformations are not found in a pure mode analogous to the bulk deformations. In order for the surface elastic term proportional to K_{24} (saddle-splay surface elastic constant) to contribute to the configuration, very specific surface and anchoring conditions are required. [It should be noted that different definitions of K_{24} have been used by various researchers; our definition is given in Eq. (1) below.] For example, the K_{24} distortion can result from liquid-crystal molecules being anchored to a curved surface [5], inhomogeneous configurations in planar cells [6], or hybrid aligned cells with degenerate parallel anchoring [7]. These systems are complicated to analyze both theoretically and experimentally which has hindered the measurement of K_{24}. The measurement of K_{24} is further aggravated by the difficulty in separating surface elastic energies from molecular anchoring energies.

Surface elastic terms are unimportant in bulk quanti-

ties of liquid crystal and typically ignored. But when liquid crystals are confined to small cavities its effect is found to be significant, particularly when elastic energies imposed by the confining volume compete with molecular anchoring energies. Polymer dispersed liquid-crystal (PDLC) droplets are systems that exhibit the K_{24} distortion. Erdmann, Zumer, and Doane [8] successfully measured the molecular anchoring strength in PDLC systems with perpendicular anchoring but were limited to large droplets ($R > 3$ μm) by optical methods where the effective anchoring strength is strong, washing out any detailed information on the surface elastic constant K_{24}. Zumer [9] has extended the theory of the PDLC systems with perpendicular boundary conditions to include the surface elastic constant K_{24}. Furthermore, Zumer has proposed several methods to determine K_{24} based on the radial-to-axial structure transition and zero-field microscopy studies of the axial structure, where the simulated microscope textures [10] are sensitive to the ratio K_{24}/K_{11} [11,12]. It was also concluded that $K_{24} < 2K_{11}$ based solely on the existence of the zero-field axial structure observed by Erdmann, Zumer, and Doane. In this contribution we study in detail nematic director configurations that exist in cylindrical geometries that simplify both the theoretical treatment and experimental analysis, allowing the determination of K_{24}.

It was first thought in the early 1970s that the nematic director field in a cylinder with perpendicular boundary conditions would consist of only a radial component with a line disclination along the cylinder axis where the director field is undefined [13] (see Fig. 1). Cladis and Kleman [14] and Meyer [15] have shown that the high cost of splay deformation energy in the center of the cylinder could be relieved by introducing a finite amount of bend deformation. This results in a continuous director field that is planar radial near the cavity wall but escapes into the third dimension along the cylinder axis (see Fig. 1). Comparison of the free energies of these two structures under strong anchoring conditions at the cavity wall revealed that the escaped-radial structure would be expected to revert to the planar-radial structure at a sufficiently small cavity radius, $R_c \approx 0.1$ μm. Optical studies verified the existence of the escaped-radial structure in large capillary tubes of radii 20–200 μm occurring with singular point defects regularly spaced along the cylinder axis [16–20]. The defects result from the fact that two energy-equivalent configurations exist where the direction of bend is changed (see Fig. 1). Kuzma and Labes [21] extended these studies to smaller radii but were limited by optical methods to cavity radii greater than 2 μm. The smectic-A [22] and cholesteric [23] phases were also studied in large capillary tubes by Cladis when perpendicular anchoring conditions exist at the surface.

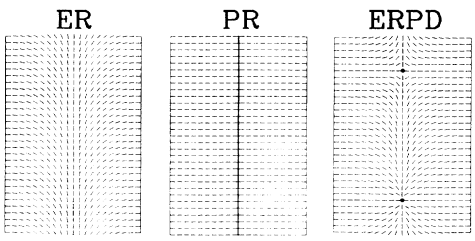

FIG. 1. Three possible nematic-director fields in capillary tubes, escaped radial (ER), planar radial (PR), and escaped radial with singular point defects (ERPD).

The most desirable way to study nematic director fields in cylindrical capillaries is by optical polarizing microscopy [15–21]. The observed optical birefringence patterns for the escaped-radial nematic director field for two orientations of the cylinder axis with respect to the initial polarization vector ($\alpha_0 = 0°$ and 45°) is presented in Fig. 2. The transmitted light at the $\alpha_0 = 0°$ orientation is essentially extinct so that the texture appears dark except near the center of the tube. The extinction results from the director field being nearly radial in this region. The maximum transmitted intensity occurs at $\alpha_0 = 45°$ where the escaped region along the axis is visible. The presence of a singular point defect along the cylinder axis is easily identified by this method. Although optical methods are the most direct way to study nematic structures, the resolution of the technique limits studies to cavity sizes greater than 2 μm. This is far larger than the size expect-

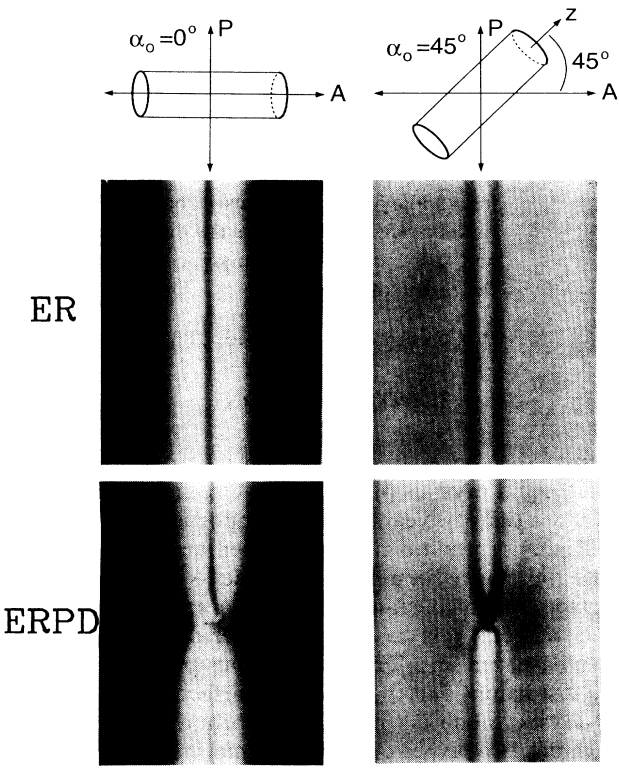

FIG. 2. Optical birefringence patterns of the escaped-radial configuration using a while-light source. The sample is prepared by filling a 200-μm-diam capillary tube treated with lecithin with the liquid-crystal compound 4'-pentyl-4-cyanobiphenyl (5CB). The continuous escaped-radial structure (a) and the escaped-radial structure with a defect (b) is presented for two orientations of the cylindrical axis with respect to the initial polarization vector ($\alpha_0 = 0°$ and 45°). For a more detailed discussion of optical microscopy studies on capillary tubes consult Refs. [15–23].

ed where the elastic energies compete with molecular anchoring energies to induce planar types of nematic director-field configurations.

More recently, nematic director configuration studies were extended to the submicrometer cylindrical cavities of Nuclepore membranes where ^{2}H-NMR was used to study the density of singular point defects that exist along the cylindrical axis of the escaped-radial configuration [24]. These results stimulated theoretical studies of multidomain configurations with perpendicular anchoring conditions at the cavity wall. Vilfan, Vilfan, and Zumer [25] predicted that under strong anchoring conditions the escaped-radial structure with alternating radial and hyperbolic defects is no longer stable for $L < L_0 \approx 0.25R$, while at larger defect separations this structure is metastable but unable to obtain the needed energy to relax to a continuous structure. Stability calculations were presented indicating that domain shrinkage is possible for $L < L_0$ through direct defect-defect interaction. Further calculations by Vilfan, Vilfan, and Zumer [25] predicted the existence of a new structure where the radial defect is replaced by a defectless axial structure which occurs when the molecular surface anchoring is diminished. This structure has yet to be observed experimentally.

In this contribution we investigate the effect of confining walls on nematic liquid crystals which introduce a variety of exciting behaviors of basic importance [26–28]. The most profound effects occur when the curvature of the confining walls introduces elastic deformations which compete with the anchoring strength at the wall surface to create nematic structures that are sensitive to the detailed elastic properties of the nematic material [29]. We present an innovative deuterium nuclear-magnetic-resonance (^{2}H-NMR) study of nematic liquid crystals confined to the cylindrical cavities of Nuclepore membranes and the involved theory behind the measurements. Cavities with untreated surfaces are found to provide an anchoring strength of sufficient magnitude to support the escaped-radial director configuration for radii as small as 0.05 μm while cavities with treated lecithin walls reveal weakened anchoring strengths and only support this structure in cavities of radius 0.5 μm and larger. When sufficiently weak anchoring conditions exist at the cavity boundary a different planar-polar configuration is observed to occur instead of the previously predicted planar-radial configuration.

The sensitivity of the ^{2}H-NMR technique to small differences in the nematic director field imposed by the curvature or elastic properties of the nematic liquid crystals are strongly reflected in the shape of the ^{2}H-NMR spectral pattern. The escaped-radial and planar-polar structures are shown to exhibit markedly different spectral patterns. Studying the escaped-radial structure in a series of cavity sizes or observing the escaped-radial to planar-polar transition point allows the measurement of both K_{24} and the molecular-anchoring strength W_0. The value of K_{24} is found to be comparable in size to splay, twist, and bend bulk elastic constants in the compound 4′-pentyl-4-cyanobiphenyl (5CB-βd_2) at room temperature based on two independent ^{2}H-NMR measurements. A stability calculation describing the observed configuration transition provides an additional estimate on the value of K_{24} that complements the NMR measurements.

The role of curvature, molecular anchoring, and surface elastic constants is not just limited to basic studies, but offers valuable information to the applied audience as well. PDLC's are attractive materials for display applications, one of these applications being projection displays where they provide bright, high-contrast images [30,31]. For PDLC materials to be successful in high-resolution systems it is necessary to adopt these materials to the active matrix which requires low driving voltages, high resistivities, and rapid response rates [32]. Engineering PDLC materials to meet these specifications requires an in-depth knowledge of the nematic director fields which occur in micrometer and submicrometer spherical cavities. While cavities of cylindrical shape do not occur in practical PDLC devices, these cylindrical geometries teach us how to create and control nematic director fields under various surface conditions and wall curvatures. The cylindrical cavities of Nuclepore membranes have two distinct advantages for studying surface effects: (1) the surfaces are accessible to chemical treatment that controls the molecular anchoring strength and anchoring angle; (2) the cylindrical symmetry simplifies the theoretical analysis of the director configuration. Many of the material and surface parameters determined in our studies can be carried over to other cavity shapes important in electrooptic devices.

II. ELASTIC CONTINUUM THEORY

The nematic director-field configuration inside a small cavity under stable conditions depends on the elastic properties of the liquid-crystal material, the strength and preferred orientation of the molecular anchoring at the cavity wall, and the strength and orientation of an applied field. The elastic free energy that describes the bulk and surface elastic character exhibited by liquid-crystal materials as described by Saupe [33] is expressed as

$$F_v = \frac{1}{2}\int_{\text{vol}} \{K_{11}(\text{div}\mathbf{n})^2 + K_{22}(\mathbf{n}\cdot\text{curl}\mathbf{n})^2 + K_{33}(\mathbf{n}\times\text{curl}\mathbf{n})^2 - K_{24}\text{div}(\mathbf{n}\times\text{curl}\mathbf{n} + \mathbf{n}\,\text{div}\mathbf{n})\}dV \,, \quad (1)$$

where the identity $\mathbf{n}\times\text{curl}\mathbf{n} = -[(\mathbf{n}\cdot\nabla)\mathbf{n}]$ is used and the order parameter S is assumed constant throughout the volume of the cavity. The nematic director $\mathbf{n}$ represents the local direction of the optic axis of the uniaxial nematic liquid crystal and K_{11}, K_{22}, and K_{33} are the phenomenological splay, twist, and bend bulk elastic constants. K_{24} is called a surface elastic constant because it enters the free energy as the coefficient of a divergence term which can be transformed to a surface integral by Green's theorem.

We have not been complete in Eq. (1) in that we have neglected the other surface term $\int_{\text{vol}} K_{13}\text{div}(\mathbf{n}\,\text{div}\mathbf{n})dV$, commonly called the mixed splay-bend contribution. This is based on having weak deformation and consistently keeping terms only of first derivatives of $\mathbf{n}$. Including K_{13} into Eq. (1) would also re-

quire the inclusion of volume elastic free energy terms which involve the square of second derivatives of the director field [26,27].

The interaction between the nematic liquid crystal and the confining surface gives rise to a surface free energy first proposed by Rapini-Papoular [34] which has the following form:

$$F_s = \frac{1}{2}\int_{\text{surf}} W_0 \sin^2\phi \, dS \ , \tag{2}$$

where ϕ is the angle between $\mathbf{n}$ and the preferred direction of alignment at the surface and W_0 denotes the strength of the interaction in units of energy per area. We will consider structures with perpendicular anchoring at the surface and therefore the normal to the surface is assumed to be the preferred anchoring direction. In the strong anchoring limit, $W_0 \rightarrow \infty$, the surface free energy is replaced by the boundary condition $\phi = 0°$ since the nematic director becomes perpendicular to the surface. It should be stressed at this point that W_0 strongly depends on the type of surface and surface treatment employed while the surface elastic constant K_{24} in Eq. (1) is a material parameter independent of any short-range interactions occurring at the surface.

The contribution to the free energy that describes the interaction of the liquid-crystal molecules with an external magnetic ($\mathbf{B}$) or electric ($\mathbf{E}$) field is described by

$$F_F = -\frac{1}{2}\int_{\text{vol}} \frac{\Delta\chi}{\mu_0}(\mathbf{B}\cdot\mathbf{n})^2 dV \tag{3a}$$

or

$$F_F = -\frac{1}{2}\int_{\text{vol}} \Delta\epsilon\epsilon_0(\mathbf{E}\cdot\mathbf{n})^2 dV \tag{3b}$$

where $\Delta\chi$ is the anisotropy in the diamagnetic susceptibility and $\Delta\epsilon$ is the anisotropy in the dielectric constant. The equilibrium configurations that follow are calculated for cylindrical geometries with perpendicular boundary conditions. All the configurations are calculated in zero field so the contribution of Eqs. (3) is not included. The influence of the magnetic field introduced by the NMR spectrometer on the nematic director-field configuration can be shown to be negligible by calculating the magnetic coherence length given by the relation $\xi_m = (\mu_0 K/\Delta\chi)^{1/2}/B$, where K is some average of elastic constants K_{ii}, depending upon the specific director configuration. Using the appropriate constants for the liquid-crystal material 5CB (4'-pentyl-4-cyanobiphenyl) and strength of the NMR magnetic field (4.7 T), the magnetic coherence length is ≈ 1.7 μm [35] which is significantly larger than the cavity radii employed in this study.

A. Planar-radial structure

The planar-radial (PR) configuration has been treated in detail by other authors [13–15] so only a brief discussion will be presented here. Since $\mathbf{n}$ is normal to the surface, the energy per unit length of the cylinder, which is pure splay energy, is given by

$$F_{\text{PR}} = \pi K_{11} \ln(R/\rho) \ , \tag{4}$$

where ρ is the radius of the line disclination which is of the order of molecular dimensions, at which elastic theory breaks down. This configuration is independent of anchoring strength since $\mathbf{n}=\mathbf{r}$. The surface elastic constant K_{24} also does not contribute to Eq. (4) because the effect of the inner surface at ρ cancels with the outer surface at R. This is given mathematically by $\text{div}(\mathbf{n}\times\text{curl}\mathbf{n}+\mathbf{n}\,\text{div}\mathbf{n}) = \delta(r)/r$ when $\mathbf{n}=\mathbf{r}$.

B. Planar-polar structure

The planar-polar (PP) structure can be specified by $\mathbf{n} = \cos\psi(r,\theta)\mathbf{r} + \sin\psi(r,\theta)\boldsymbol{\theta}$ where ψ is the angle between the local nematic director and the radial direction as illustrated in Fig. 3(a). If the simplifying assumption that $K_{11} = K_{33} \equiv K$ is made, the Euler-Lagrange equation for minimizing the elastic free energy then becomes the Laplace equation in two dimensions (the polar coordinates r and θ)

$$\frac{d^2\psi(r,\theta)}{dr^2} + \frac{1}{r}\frac{d\psi(r,\theta)}{dr} + \frac{1}{r^2}\frac{d^2\psi(r,\theta)}{d\theta^2} = 0 \ . \tag{5}$$

The exact solution in the strong anchoring limit to Eq. (5) can be found by applying the appropriate boundary conditions $\psi(R,\theta)=0$, $\psi(r,0)=\pi/2$, and $\psi(r,\pi/2)=0$ and employing a conformal mapping technique to obtain the solution

$$\psi(r,\theta) = \tan^{-1}\left\{\frac{R^2-r^2}{(R^2+r^2)\tan\theta}\right\} = \frac{\pi}{2} - \tan^{-1}\left\{\frac{(R^2+r^2)}{(R^2-r^2)}\tan\theta\right\} \ . \tag{6}$$

One can immediately see that K_{24} does not contribute to this configuration since $\text{div}(\mathbf{n}\times\text{curl}\mathbf{n}+\mathbf{n}\,\text{div}\mathbf{n}) = 0$. In fact, the term in Eq. (1) proportional to K_{24} is identically zero for any planar configuration in cylindrical geometries independent of the anchoring direction at the cavity wall. The free energy per unit length of the cylinder is determined to be

$$F_{\text{PP}} = \pi K \ln(R/2\rho) \ , \tag{7}$$

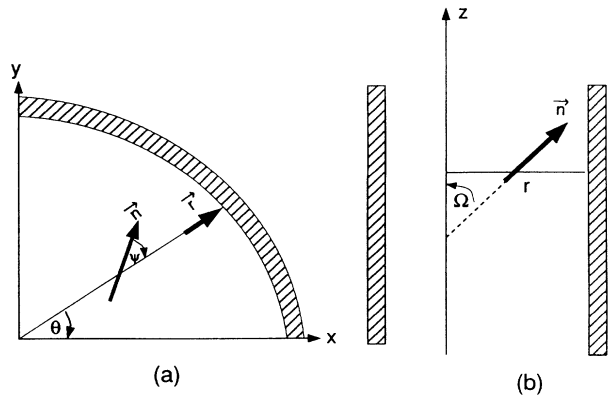

FIG. 3. Schematic representation of the coordinate systems used in the text for the planar-polar (a) and escaped-radial (b) structures.

where ρ is the radius of the axial line disclinations centered at $r=R$, $\theta=0$, and π. The line disclinations in the PR and PP configurations are introduced to avoid an infinity in the free energy arising due to the breakdown of elastic theory. A more accurate description of the physics would include spatial variations of the local degree of orientational order [36].

If weak anchoring occurs at the surface, the boundary condition $\psi(r=R)=0$ is relaxed by the relation

$$\left\{ W_0 \sin\psi(r,\theta)\cos\psi(r,\theta) + K\frac{d\psi(r,\theta)}{dr} \right\}\Bigg|_{r=R} = 0 \ . \tag{8}$$

The exact solution to the Euler-Lagrange equation is then given by

$$\psi(r,\theta) = \frac{\pi}{2} - \tan^{-1}\left\{ \frac{(R^2+\gamma r^2)}{(R^2-\gamma r^2)}\tan\theta \right\} , \tag{9}$$

where $\gamma=(\xi^2+1)^{1/2}-\xi$ and $\xi=2K/RW_0$. The nematic director field is driven by the value of the effective anchoring strength RW_0/K, where it strongly influences the molecular-anchoring angle at the cavity wall as shown in Fig. 4. The free energy per unit length of the cylinder is given by

$$F_{\rm PP} = \pi K\left\{ -\ln(2\xi\gamma) + (1-\gamma)/\xi \right\} . \tag{10}$$

It can be shown by comparing Eq. (10) to Eq. (7) that the crossover to the strong anchoring regime occurs when $W_0 \sim 2K/\rho e$.

The calculation of the PP configuration becomes more involved when $K_{11} \neq K_{33}$. There is no analytical solution for this situation and therefore the resulting differential equation must be solved numerically.

C. Escaped-radial structure

The escaped-radial (ER) configuration has been studied by other authors [14,15] in the strong anchoring limit, neglecting surface elastic contributions. The nematic director is completely specified by $\mathbf{n}=\cos\Omega(r)\mathbf{z}+\sin\Omega(r)\mathbf{r}$, where Ω is the angle between $\mathbf{n}$ and the cylinder axis, and only depends on the radial variable r as illustrated in Fig. 3(b). We now carefully reexamine the ER structure to incorporate the term proportional to K_{24}, which yields

$$\mathrm{div}(\mathbf{n}\times\mathrm{curl}\mathbf{n}+\mathbf{n}\cdot\mathrm{div}\mathbf{n}) = \frac{2}{r}\frac{d\Omega(r)}{dr}\sin\Omega(r)\cos\Omega(r) \ . \tag{11}$$

The free energy per unit length of the cylinder is

$$F_{\rm ER} = \pi\int_0^R dr\, r\left\{ \frac{K_{11}\sin^2\Omega(r)}{r^2} + \left[\frac{d\Omega(r)}{dr}\right]^2 [K_{11}\cos^2\Omega(r)+K_{33}\sin^2\Omega(r)] + \frac{2(K_{11}-K_{24})}{r}\frac{d\Omega(r)}{dr}\sin\Omega(r)\cos\Omega(r) \right\} + \pi R W_0 \cos^2\Omega(r=R) \ . \tag{12}$$

The term proportional to $(K_{11}-K_{24})$ is a total differential that can be integrated exactly to obtain

$$F_{\rm ER} = \pi\int_0^R dr\, r\left\{ \left[\frac{d\Omega(r)}{dr}\right]^2 [K_{11}\cos^2\Omega(r)+K_{33}\sin^2\Omega(r)] + \frac{K_{11}\sin^2\Omega(r)}{r^2} + \pi(K_{11}-K_{24}) \right\} + \pi\{RW_0+K_{24}-K_{11}\}\cos^2\Omega(r=R) = 0 \ . \tag{13}$$

Minimization of Eq. (13) results in the following differential equation:

$$\frac{d^2\Omega(r)}{dr^2}\{K_{11}\cos^2\Omega(r)+K_{33}\sin^2\Omega(r)\} + \left[\frac{d\Omega(r)}{dr}\right]^2 \sin\Omega(r)\cos\Omega(r)\{K_{33}-K_{11}\} + \frac{1}{r}\frac{d\Omega(r)}{dr}\{K_{11}\cos^2\Omega(r)+K_{33}\sin^2\Omega(r)\} - \frac{K_{11}}{r^2}\sin\Omega(r)\cos\Omega(r) = 0 \ . \tag{14}$$

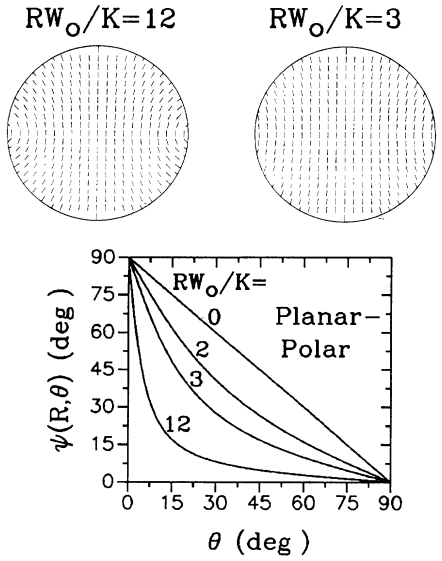

FIG. 4. The effect of the dimensionless surface parameter RW_0/K on the planar-polar configuration for $K_{11}=K_{33}\equiv K$. The diagram shows the dependence of the molecular-anchoring angle at the cavity wall in terms of the polar coordinate θ for various anchoring regimes.

The solution in the strong anchoring limit $\Omega(r=R)=\pi/2$ and one-constant approximation is given by the expression

$$\Omega(r)=2\tan^{-1}(r/R) , \tag{15}$$

which is identical to the previously reported solutions, except the free energy now becomes

$$F_{ER}=\pi K(3-K_{24}/K) , \tag{16}$$

where the K_{24} distortion contributes to the free energy.

If weak anchoring occurs at the surface, the boundary condition $\Omega(r=R)=\pi/2$ can be replaced by the relation

$$\left[\frac{d\Omega(r)}{dr}\right]\Bigg|_{r=R}=\left[\frac{\sin\Omega(r)\cos\Omega(r)(RW_0+K_{24}-K)}{KR}\right]\Bigg|_{r=R} . \tag{17}$$

The solution to Eq. (14) becomes

$$\Omega(r)=2\tan^{-1}\left[\frac{r}{R}\tan(\alpha/2)\right] , \tag{18}$$

where α is the molecular-anchoring angle at the surface given by the relation

$$\alpha=\Omega(r=R)=\cos^{-1}(1/\sigma) . \tag{19}$$

The dimensionless surface parameter σ governs the anchoring regime and is defined by

$$\sigma=\frac{RW_0}{K}+\frac{K_{24}}{K}-1 . \tag{20}$$

Equations (18) and (19) are valid when $\sigma>1$. If the physical parameters are such that $\sigma<1$ then $\Omega=0$ everywhere. The presence of a finite σ tilts the molecular-anchoring angle away from its preferred perpendicular orientation as shown in Fig. 5. In the strong anchoring limit $\sigma\rightarrow\infty$, resulting in $\alpha\rightarrow\pi/2$ reducing Eq. (18) to Eq. (15) where strong anchoring is implied. One can see by Eq. (20) that K_{24} strongly influences the nematic director field in the weak anchoring regime when K_{24}/K is comparable to RW_0/K. In the case of very weak anchoring ($\sigma<1$), the molecular-anchoring angle at the surface reduces to a parallel orientation along the cylinder axis. However, the director field would probably revert to the planar-polar configuration before this situation is realized. The free energy per unit length is given by

$$F_{ER}=\begin{cases}\pi K(3-K_{24}/K-1/\sigma), & \sigma>1\\ \pi K(RW_0/K), & \sigma<1 .\end{cases} \tag{21}$$

It is important to point out that the K_{24} term contributes to the free energy given by Eq. (21) independent of the anchoring regime. Therefore one must be careful in neglecting the K_{24} distortion based solely on the strong anchoring assumption, particularly when free-energy considerations are involved.

If weak anchoring occurs at the surface and $K_{11}\neq K_{33}$, the solution to Eq. (14) must be reconsidered. The boundary condition at the surface is given by the relation

$$\frac{d\Omega(r)}{dr}\Bigg|_{r=R}=\frac{(RW_0+K_{24}-K_{11})\sin\alpha\cos\alpha}{R(K_{11}\cos^2\alpha+K_{33}\sin^2\alpha)} . \tag{22}$$

The molecular-anchoring angle at the cavity wall is given by the expression

$$\alpha=\Omega(R)=\cos^{-1}\left[\frac{k^{1/2}}{(\sigma^2+k-1)^{1/2}}\right] , \tag{23}$$

where $k=K_{33}/K_{11}$ and the dimensionless surface parameter σ is now defined as

$$\sigma=\frac{RW_0}{K_{11}}+\frac{K_{24}}{K_{11}}-1 , \tag{24}$$

which is the same definition as in Eq. (20) except K is replaced by K_{11}. The exact solution to Eq. (14) is solved for two cases: $k>1$ and $k<1$, yielding the relations

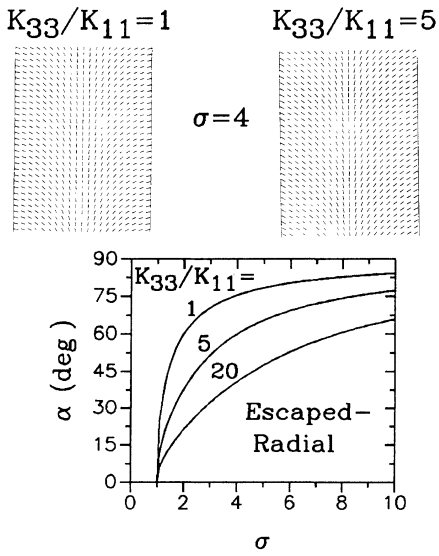

FIG. 5. The response of the escaped-radial configuration in the presence of a finite σ for different values of K_{33}/K_{11}. The diagram reveals the behavior of the molecular-anchoring angle at the cavity wall in terms of the surface parameter σ for several values of the bend-to-splay ratio.

$$\frac{r}{R}=\left[\frac{\sigma+1}{\sigma-1}\right]^{1/2}\left[\frac{\Delta-\beta'\cos\Omega(r)}{\Delta+\beta'\cos\Omega(r)}\right]^{1/2}\times\exp\left\{\frac{\beta}{\beta'}\sin^{-1}(\beta\cos\alpha)\right\}\times\exp\left\{-\frac{\beta}{\beta'}\sin^{-1}[\beta\cos\Omega(r)]\right\},\quad k>1 \tag{25}$$

and

$$\frac{r}{R}=\left[\frac{\sigma+1}{\sigma-1}\right]^{1/2}\left[\frac{\Delta-\beta'\cos\Omega(r)}{\Delta+\beta'\cos\Omega(r)}\right]^{1/2}\times\exp\left\{-\frac{\beta}{\beta'}\sinh^{-1}(\beta\cos\alpha)\right\}\times\exp\left\{\frac{\beta}{\beta'}\sinh^{-1}[\beta\cos\Omega(r)]\right\},\quad k<1 \tag{26}$$

where $\Delta=[1-\beta^2\cos^2\Omega(r)]^{1/2}$, $\beta^2=|k-1|/k$, and $\beta'^2=1/k$. The effect of a finite σ and increasing values of K_{33}/K_{11} on the nematic director field is presented in Fig. 5 along with the dependence of the molecular-anchoring angle at the cavity wall in terms of the dimensionless surface parameter σ. It is interesting to demonstrate the response of the equilibrium configuration for increasing values of K_{33}/K_{11} in different anchoring regimes. In the strong anchoring limit ($\sigma\rightarrow\infty$), the directors relieve the expensive bend deformation by introducing more splay into the system (see Fig. 6) as K_{33}/K_{11} increases. However, in the presence of finite anchoring ($\sigma=4$), the system alleviates the high cost of bend in quite a different manner. Increasing the value of K_{33}/K_{11} decreases the molecular anchoring angle of the director at the cavity wall (see Fig. 6). Therefore both anchoring regimes relieve the costly bend by reducing the escaped region in the center through two very different mechanisms. The free energies per unit length are given by the relations

$$F_{\rm ER}(k>1)=\pi K_{11}\left\{2+\frac{k}{\sqrt{k-1}}\tan^{-1}\sqrt{(k-1)}-\frac{k}{\sqrt{k-1}}\tan^{-1}\left[\frac{\sqrt{k-1}}{\sigma}\right]-\frac{K_{24}}{K_{11}}\right\} \tag{27}$$

and

$$F_{\rm ER}(k<1)=\pi K_{11}\left\{2+\frac{k}{\sqrt{1-k}}\tanh^{-1}\sqrt{(1-k)}-\frac{k}{\sqrt{1-k}}\tanh^{-1}\left[\frac{\sqrt{1-k}}{\sigma}\right]-\frac{K_{24}}{K_{11}}\right\}. \tag{28}$$

The free energy per unit length in terms of K_{33}/K_{11} is presented in Fig. 7. This demonstrates that positive values of K_{24}/K_{11} lowers the free energy independent of the anchoring regime.

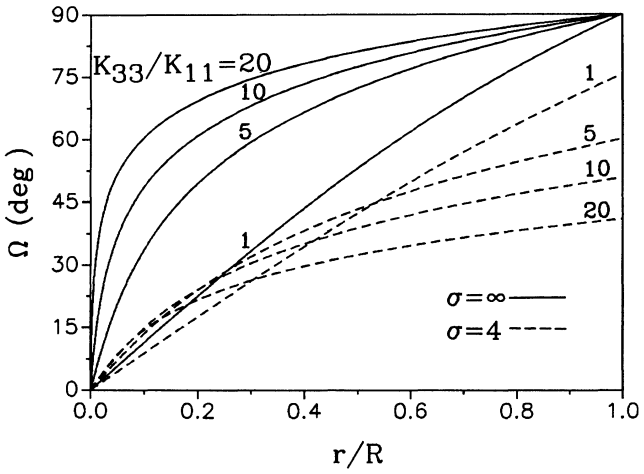

FIG. 6. The equilibrium distribution for the escaped-radial structure in the strong ($\sigma=\infty$) and weak ($\sigma=4$) anchoring limits for increasing values of K_{33}/K_{11}. The response of the configuration to alleviate the expensive bend deformation strongly depends on the anchoring regime. The value of K_{33}/K_{11} plays a vital role in determining the molecular-anchoring angle at the cavity wall ($r/R=1$) in the weak anchoring regime.

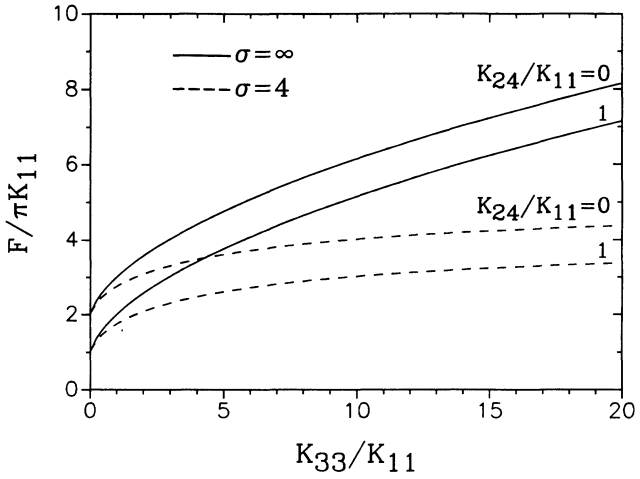

FIG. 7. The free energy per unit length of the escaped-radial configuration for two values of the saddle-splay surface elastic constant in the strong and weak anchoring regimes.

D. Escaped radial with point defects

In reality, a continuous ER structure is seldom realized when the liquid-crystal material is cooled from the isotropic fluid phase into the orientationally ordered nematic phase. Fluctuations that are intrinsic near the nematic-isotropic transition and irregularities of the cavity walls often lead to a partially escaped structure. Examination of the ER structure indicates that the director can escape either towards $z>0$ or $z<0$. If these two situations occur in different regions of the same cylinder, singular

point defects of two types occur along the cylinder axis: radial and hyperbolic creating an escaped-radial structure with point defects (ERPD) [19,20,24,25,37]. It is periodic in the z direction with period $2L$, which is the distance between two defects of the same type. This structure is much more difficult to treat analytically even in the one-constant approximation since Ω depends both on the radial and axial coordinates giving rise to the Euler equation

$$\frac{d^2\Omega(r,z)}{dr^2}+\frac{1}{r}\frac{d\Omega(r,z)}{dr}+\frac{d^2\Omega(r,z)}{dz^2}-\frac{1}{r^2}\sin\Omega(r,z)\cos\Omega(r,z)=0 . \quad (29)$$

Therefore we resort to a trial function that satisfies all the necessary boundary conditions. The solution must approximate the director near the radial point defect at $r=z=0$, given by the expression

$$\Omega(r,z)=\tan^{-1}(r/z) , \quad (30)$$

and the director near the hyperbolic defect at $z=L$, $r=0$, given by the expression

$$\Omega(r,z)=\tan^{-1}\left[\frac{r}{1-z/L}\right] . \quad (31)$$

The above forms describe the director in regions near the defects but fail to satisfy the boundary conditions at the surface of the cylinder which are the same as for the ER configuration. Restricting our interest to the region $L/R<2$ and $\sigma>1$, a trial function that has the desired defects given by Eqs. (30) and (31) and satisfies the boundary conditions is given by the relation

$$\Omega(r,z)=\tan^{-1}\left\{\frac{\sigma r}{z(1-z/L)(\sigma-[\sigma-1]r/R)}\right\} \quad (32)$$

for a cell $r\le R$ and $0\le z\le L$. A point in the region $-L\le z\le 0$, which makes up the other half of the unit cell, has an angle Ω that is the supplement of the angle at the corresponding point in the region $0\le z\le L$, i.e., $\Omega(-z)=\pi-\Omega(z)$. Periodic repetition of the cell produces a lattice of alternating radial and hyperbolic defects of spacing L which is in close agreement with numerical studies [25,37]. The ERPD structure is plotted in Fig. 8 for various values of σ at a constant defect density along with the dependence of the molecular-anchoring angle on the axial coordinate. The resulting free energy per unit length can be approximated by the expression

$$F_{\rm ERPD}=\pi K\left\{-\tfrac{4}{3}\ln(L/R)+3-\frac{K_{24}}{K}+\frac{8}{9}+\frac{1}{3\sigma}+\frac{1}{6\sigma^2}+\frac{\pi}{5}\left[\frac{\sigma-1}{\sigma}\right]\frac{L}{R}\cdots\right\} . \quad (33)$$

These trial functions are valid for $L/R<2$.

E. Nematic director-field configuration transitions

It was previously predicted that the ER structure would transform into the PR structure at the critical radius $R_c\rho e^3$ [14,15], but closer examination of the free energies for the planar structures summarized in Table I reveals that the PP structure is always energetically favorable over the PR structure provided the line disclinations have the same radius ρ and $K_{11}\sim K_{33}$. Therefore we expect the PP structure to occur instead of the PR structure at small radii. A phase diagram is presented in Fig. 9 in terms of the dimensionless variable RW_0/K clearly identifying the regions of stability for the PP and ER configurations. This diagram is particularly useful in determining the magnitude of K_{24}, based on the configuration transition since K_{24} enters into the effective anchoring strength for the ER configuration, while the PP structure depends only on RW_0/K and is independent of K_{24}. A phase diagram is presented in Fig. 10 that predicts the regions of stability for the PP and ER configurations in terms of the dimensionless parameters RW_0/K and K_{24}/K.

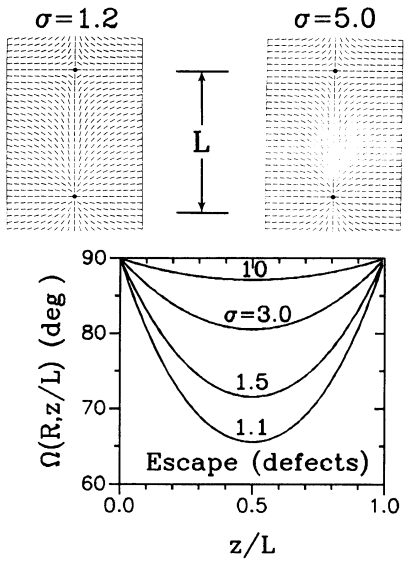

FIG. 8. The effect of the surface parameter σ on the escaped-radial configuration with singular point defects. The diagram reveals the profile of the molecular-anchoring angle between successive point defects.

Many experimental studies have revealed the existence of singular point defects along the cylinder axis [16–20,24,29,37,38]. Although the $F_{\rm ERPD}$ is greater than $F_{\rm ER}$, the point defects of real samples are typically unable to relax by going to the ends of the cylinder. The boundary conditions on the ends are expected to repel them, resulting in array of equally spaced defects. The precise value of R at which the ERPD configuration crosses over to the PP configuration is difficult to predict because of the uncontrollable parameter L/R. However, experimentally in submicrometer cavities, the defect density is found to be in the range $1.5R\le L\le 2.0R$ [24,29,37], which is consistent with predictions [25].

F. Conditions under which K_{24} is important

The surface elastic term proportional to K_{24} in the elastic free-energy expression given by Eq. (1) is nonzero

TABLE I. Summary of free energies for nematic director-field configurations in cylindrical geometries with perpendicular anchoring conditions in the one-constant approximation.

Configuration	Strong	Weak
Planar Radial (PR)	$\pi K_{11}\ln(R/\rho)$	
Planar Polar (PP)	$\pi K\ln(R/2\rho)$	$\pi K\{-\ln(2\xi\gamma)+(1-\gamma)/\xi\}$ $\gamma=(\xi^2+1)^{1/2}-\xi$ $\xi=\frac{2K}{W_0R}$
Escaped Radial (ER)	$\pi K\left[3-\frac{K_{24}}{K}\right]$	$\pi K\left[3-\frac{K_{24}}{K}-\frac{1}{\sigma}\right]$ $\sigma=\frac{RW_0}{K}+\frac{K_{24}}{K}-1$ $\sigma>1$

only when the director depends on more than one Cartesian coordinate. Therefore previous studies on planar surfaces in which the director is homogeneously aligned or homeotropically aligned were valid in neglecting the K_{24} term when **n** depends only on the coordinate normal to the surface. However, the role of curvature introduced by cylindrical [14–25,29,37,38] or spherical [5,8–10,12,39] confinement or samples with inhomogeneous configurations such as stripes [6] should be analyzed in terms of the free energy that includes the K_{24} term. It was recently reported [7] that hybrid aligned samples with degenerate parallel anchoring have the K_{24} distortion. An estimate value of K_{24} was determined based on stability calculations of structures observed with optical microscopy.

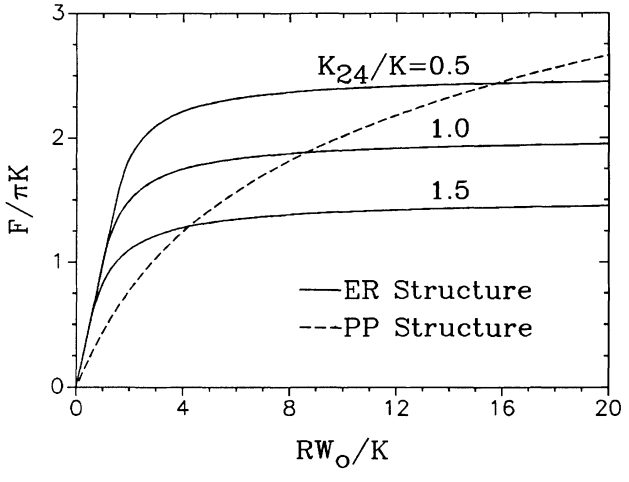

FIG. 9. Free energy per unit length in terms of molecular-anchoring strength for the planar-polar (PP) and escaped-radial (ER) structures in the one-constant approximation. The intersection point predicts the value of RW_0/K where the structural transition occurs.

III. PRINCIPLE OF DEUTERIUM NMR MEASUREMENTS

^{2}H-NMR is a particularly convenient technique to probe nematic structures [24,29,37,39–42] since this method gives the distribution of the director orientation inside the cavity for all cavity sizes. The characteristic features of the ^{2}H-NMR line shapes of confined nematic structures are the width and shape of the spectral patterns. Assuming that the order parameter S is constant throughout the volume of the cylinder, i.e., there is no evidence that ^{2}H-NMR is sensitive to the change of orientational order near the cavity wall or defect regions in the *nematic* phase, the line shape and linewidth depend on three factors: (1) the nematic structure inside the cylinder, (2) the orientation of the cylinder axis in the magnetic field, and (3) to a small extent translational

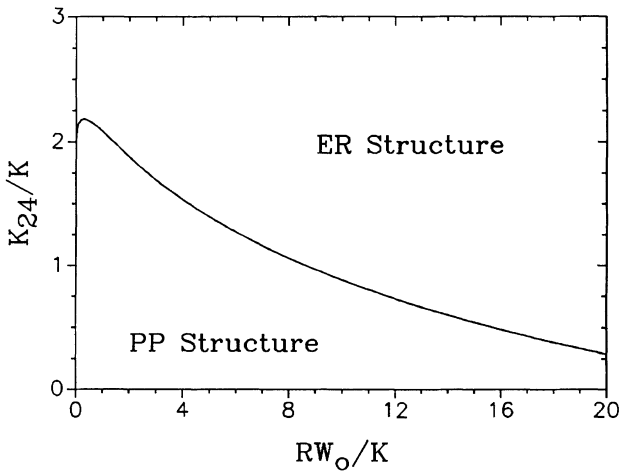

FIG. 10. Calculated regions of stability for the planar-polar (PP) and escaped-radial (ER) structures in the one-constant approximation.

self-diffusion. Since the resonance frequency depends on the angle between the nematic director **n** and the magnetic field **B**, the ^{2}H-NMR spectrum is sensitive to the nematic director distribution inside the cavity. The nematic director configuration is investigated at two orientations of the cylinder axis in the magnetic field: parallel ($\theta_B=0°$) and perpendicular ($\theta_B=90°$) for more precise structure determination.

The extent of motional averaging can be estimated by the simple diffusion relation $x_0 \sim \sqrt{D/\delta\nu}$, where D is the diffusion constant, $\delta\nu$ is the quadrupole splitting, and x_0 is the distance the molecule migrates during the NMR measurement. Using typical values for the diffusion constant $D \sim 10^{-11}$ m^2/s and $\delta\nu \sim 40$ kHz, the molecule diffuses on the average of $x_0 \sim 0.02$ μm which is smaller than the smallest cylinder radius used in these studies. Diffusion is expected to have only minor effects on the spectrum since the range the molecule diffuses on the NMR time scale is small compared to the distance the director orientation changes appreciably [24]. In contrast the influence of diffusion becomes extremely important when considering surface-induced orientational order in the isotropic phase because the molecules sample wide variations of order during the NMR measurement [43,44].

In a local region of the cylinder represented by the position vector **r**, a compound selectively deuterated at a specific site on the molecule will yield a spectrum of two lines at quadrupole frequencies $\delta\nu$, given by the relation [42]

$$\delta\nu(\mathbf{r})=\pm\frac{\delta\nu_B}{2}[3\cos^2\theta(\mathbf{r})-1] , \tag{34}$$

where $\theta(\mathbf{r})$ expresses the orientation of the local nematic director relative to the magnetic field, $\delta\nu_B$ is the quadrupole splitting of the bulk nematic phase given by $\delta\nu_B=3e^2qQS/2h$, eq is the electric-field gradient created by the carbon-deuterium (C—D) bond, eQ is the nuclear quadrupole moment, and $S=\frac{1}{2}\langle 3\cos^2\eta-1\rangle$ is the degree of orientational order of the C—D bond direction with respect to the magnetic field. It can be seen from Eq. (34) that the resonance frequency depends on the orientation of the magnetic field in the principal axis frame (director frame) in the phase. In the case of a macroscopically aligned sample, only two absorption lines are expected. This is the case when the directors of a nematic liquid crystal with positive diamagnetic susceptibility align parallel to the field. In the case when the directors are not uniformly aligned in the magnetic field but exhibit a specific director configuration as a result of boundary conditions imposed by a confining geometry, the ^{2}H-NMR line shape will reflect the distribution of directors in the sample [24,29,37,39–41].

The ^{2}H-NMR spectral distributions are simulated from the free induction decay (FID) which is a relaxation function describing the attenuation of nuclear magnetization in the time domain. The FID is described in terms of the resonance frequency expressed by Eq. (34) given by the relation [45]

$$G(t)=\left\langle \exp\left[i\int_0^t \pi\delta\nu[\mathbf{r}(t')]dt'\right]\right\rangle = \sum_j \exp[i\pi\delta\nu(r_j)t]P(r_j) , \tag{35}$$

where the time interval $(0,t)$ is divided into equal parts, $\langle\ \rangle$ represents the ensemble average, and P is the time-independent probability that there is a molecule with frequency $\delta\nu$ at position r_j. The frequency spectrum is obtained by the Fourier transformation of Eq. (35) given by

$$I(\delta\nu)=\int_{-\infty}^{\infty} G(t)\exp(-i\pi\delta\nu t)dt . \tag{36}$$

Line broadening is included by convoluting $I(\omega_q)$ with the Gaussian distribution function. Motional averaging can be included if necessary by considering an instantaneous value of the quadrupole frequency and time-dependent probability in Eq. (35) [24,39,43].

Now we will consider the ^{2}H-NMR spectral line shapes for the configurations presented in Sec. II to illustrate the effectiveness of the ^{2}H-NMR technique to probe various nematic structures with perpendicular boundary conditions. The spectral patterns are simulated in the strong anchoring limit for parallel ($\theta_B=0°$) and perpendicular ($\theta_B=90°$) orientations of the cylinder axis in the magnetic field. The resulting simulations are presented in Fig. 11. The PR configuration is trivial for the $\theta_B=0°$ orientation resulting in the situation where all the directors are perpendicular to the magnetic field. This results in two singularities separated by $\frac{1}{2}\delta\nu_B$ that correspond to the contribution from molecules with their principal axis oriented at an angle $\theta=90°$. In the $\theta_B=90°$ case, the angle θ is uniformly distributed in a cylindrical distribution

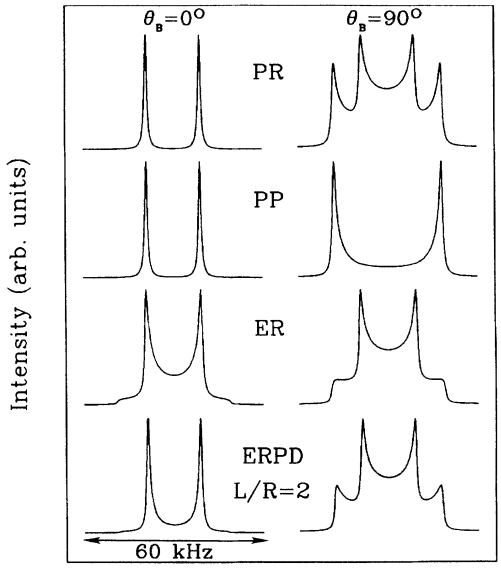

FIG. 11. Simulated ^{2}H-NMR spectral patterns for nematic configurations in a cylindrical environment where the nematic director is strongly anchored perpendicular to the cavity wall in the one-constant approximation.

giving rise to the classical ^{2}H-NMR spectral pattern for a cylindrical distribution. This is the same pattern that would be obtained for the cholesteric liquid-crystal phase where the pitch axis is oriented perpendicular to the magnetic field [46]. The PP structure yields the same spectral pattern for the $\theta_B=0°$ case as did the PR structure because all directors are perpendicular to the magnetic field, but the $\theta_B=90°$ case results in two singularities separated by $\delta\nu_B$ from the contribution of directors with their principal axis oriented at an angle $\theta=0°$. The center portion of the spectrum represents the nonzero contribution of directors in the magnetic field. The $\theta_B=90°$ orientation was calculated for the situation where the symmetry axis of the configuration aligns parallel to the magnetic field which is experimentally reported to occur when anchoring of the nematic director is sufficiently weak at the cavity wall [29].

The $\theta_B=0°$ orientation of the ER structure is characterized by two shoulders and two singularities separated by $\frac{1}{2}\delta\nu_B$. The singularities correspond to the contribution of directors orientated at $\theta=90°$ and the orientation with $\theta=0°$ contributes to the intensity of the shoulders. The $\theta_B=90°$ orientation results in a spectral pattern similar to a cylindrical distribution except the outer singularities are suppressed because of the escaping directors along the cylinder axis that contribute to the $\theta=90°$ singularities. The ERPD configuration yields two singularities separated by $\frac{1}{2}\delta\nu_B$ with a contribution in the central region of the spectrum for the $\theta_B=0°$ orientation of the cylinder axis. This is similar to the ER structure except that the shoulders are suppressed due to the presence of defects which introduce radial domain walls separated by a distance L. The $\theta_B=90°$ orientation yields a spectral pattern very similar to the cylindrical pattern with the outer singularities having a greater intensity than the ER configuration but less intense than the PR configuration. As the L approaches large values, the ERPD spectral pattern approaches that of the ER spectral pattern. Figure 11 demonstrates the utility of ^{2}H-NMR to distinguish between nematic director-field configurations that occur in cylindrical cavities with perpendicular anchoring conditions at the cavity wall.

To illustrate the sensitivity of the ^{2}H-NMR technique to the molecular-anchoring angle, consider the ER configuration described by Eq. (18) and presented in Fig. 5. Several spectra were simulated for various values of the dimensionless surface parameter σ given by Eq. (20) and are presented in Fig. 12. First consider the $\theta_B=0°$ orientation of the cylinder axis. As σ decreases, i.e., due to competition between the elastic and surface energies, the molecular-anchoring angle tilts away from its preferred anchoring direction shifting in the $\theta=90°$ singularities to the actual anchoring angle given by Eq. (19). There is also an increase in the intensity in the shoulders due to a larger contribution of directors escaping along the cylinder axis. The $\theta_B=90°$ orientation results in the suppression of the $\theta=0°$ contribution as σ decreases due to the increased number of directors escaping along the cylinder axis contributing to the $\theta=90°$ singularities. The spectra will eventually reduce to two sharp singularities for the trivial case where the directors align parallel to the cylinder axis for $\sigma<1$.

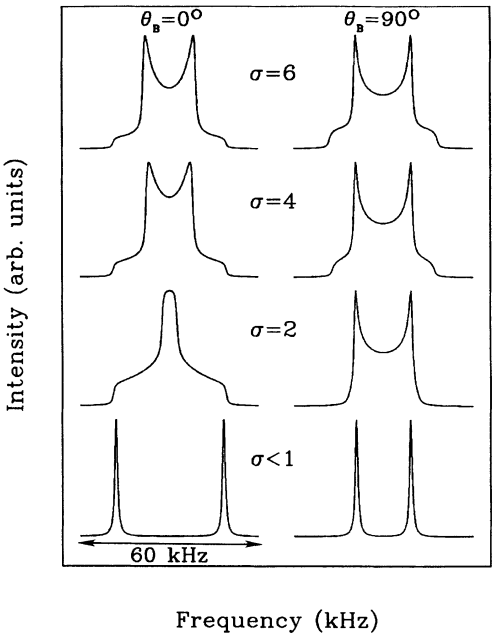

FIG. 12. Simulated ^{2}H-NMR spectral patterns for the escaped-radial configuration for various values of the dimensionless surface parameter σ when $K_{11}=K_{33}\equiv K$.

The ERPD spectral patterns behave in a similar manner except the sensitivity to σ is less pronounced. This can be seen in Fig. 13 where the trial function given by Eq. (32) is used. For small values of σ the $\theta=90°$

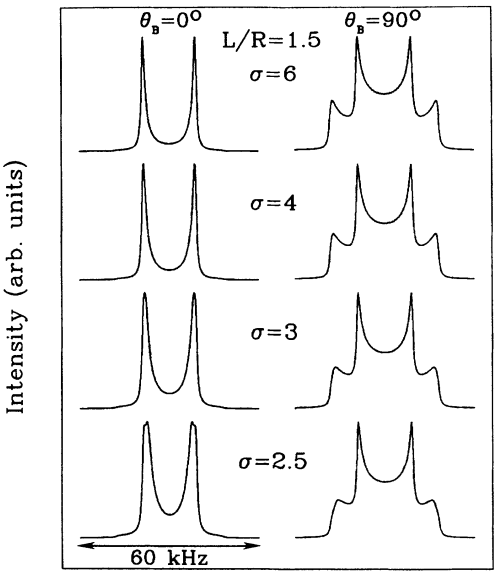

FIG. 13. Simulated ^{2}H-NMR spectral patterns for the escaped-radial configuration with alternating radial and hyperbolic defects at constant defect density $L/R=1.5$ for various values of the dimensionless surface parameter σ.

singularities begin to split into two resolvable peaks for the $\theta_B = 0°$ case as a result of the molecular-anchoring angle tilting away from the surface normal. The $\theta = 0°$ shoulders become suppressed in the $\theta_B = 90°$ case as σ is decreased. These simulations using the trial function given by Eq. (32) for the ERPD structure agree well with numerical simulations [24,37].

The PP structure described by Eq. (9) is sensitive to the anchoring parameter RW_0/K only for the $\theta_B = 90°$ orientation while the $\theta_B = 0°$ is insensitive to the anchoring strength always yielding two singularities separated by $\frac{1}{2}\delta\nu_B$. The center contribution of the PP configuration in the $\theta_B = 90°$ orientation (see Fig. 11) will reduce to two sharp singularities separated by $\delta\nu_B$ for sufficiently weak anchoring conditions as $RW_0/K \rightarrow 0$. The height of the finite contribution in the center is thus a measure of the anchoring strength assuming the symmetry axes are aligned in the field.

IV. MATERIALS

In order for nematic director configurations that exist in submicrometer cylindrical cavities to be accessible with ^{2}H-NMR, materials that offer a large surface-to-volume ratio must be realized to obtain a sufficient signal-to-noise ratio for a NMR experiment. The cavities of Nuclepore membranes [47] are very satisfying for our studies since they offer a reasonable porosity and concise cylindrical pores. The pores can be obtained in a variety of sizes ranging from 0.0075 to 6.0 μm in radii. We have studied cavities of radii 0.05 to 0.5 μm large enough for a reasonable signal-to-noise ratio yet small enough so that the magnetic field does not distort the nematic director-field.

The Nuclepore membrane is composed of a polycarbonate film with cylindrical pores penetrating through its 10-μm thickness [48]. The pores are perpendicular to the membrane surface as shown by the scanning electron microscope photograph in Fig. 14. The membranes were cut into 4-mm-wide strips and wetted with a small amount of 4'-pentyl-4-cyanobiphenyl (5CB-βd_2) [49]. They are then taken above the nematic-isotropic transition temperature (35 °C) for 1 h to ensure complete wetting of the cylindrical pores. To remove the excess liquid crystal from the surface, the membranes are pressed between two Whatmann filtration papers. Approximately 200 uniformly stacked strips are needed to perform the NMR experiments.

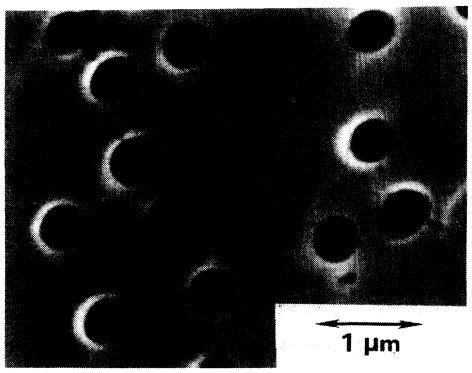

FIG. 14. Scanning electron microscope (SEM) photograph of a Nuclepore membrane with pores of radius 0.4 μm.

The principal application of Nuclepore membranes is critical filtration procedures requiring low absorption [50]. However these membranes are not new to the field of physics. They have found their way into low-temperature physics laboratories [51,52] in the study of superfluid helium, specifically used to achieve a confining geometry to study the effect of finite size near the superfluid transition. The membranes were first introduced to the liquid-crystal community by Kuzma and Labes [21] who performed microscopy studies to investigate director configurations and finite-size effects. Recently it was demonstrated that deuterium NMR is sensitive to the surface-induced nematic order imposed by the cavity walls of Nuclepore membranes of an isotropic liquid crystal [43].

The ^{2}H-NMR experiments were performed on a home-built coherent pulsed spectrometer specifically designed for structure determination and phase-transition studies of liquid-crystalline materials. A modified quadrupolar echo sequence $(\pi/2)_x$-τ-$(\pi/2)_y$ was used where $\tau = 100$ μs and the length of the $\pi/2$ pulse was 5 μs. The FID was averaged 10 000–50 000 times depending on the cavity size of the sample. Smaller cavity sizes require additional averaging since there is less deuterated material present in the sample. The temperature is regulated by a circulating fluid bath with resolution of 0.1 °C and sample stability of 0.05 °C. All experiments in this study were performed at room temperature. The sample is constructed such that when placed in the magnetic field all cylinders are oriented with their long axis parallel to the field ($\theta_B = 0°$) and can be rotated through 90° with a stepper motor such that the long axis of the cylinders are perpendicular ($\theta_B = 90°$) to the field.

V. DETERMINATION OF K_{24} AND W_0

^{2}H-NMR spectra were measured for a variety of cavity radii for two different surface conditions that provide perpendicular anchoring at the cavity walls: untreated and lecithin treated Nuclepore cavities filled with 5CB-βd_2. We present the methodology for separating the surface elastic constant K_{24} from the molecular-anchoring strength W_0that to date has been an experimental challenge.

The ^{2}H-NMR spectra were recorded for three samples with cavity radii 0.2, 0.1, and 0.05 μm at 24 °C for two orientations of the cylinder axis. The experimental spectra (solid curve) are presented in Fig. 15 where the dashed curve denotes the theoretical simulation. These spectra are characteristic of the ERPD structure where the details of their shape strongly depend on the surface parameter σ given by Eq. (20). The simulations are performed using Eq. (32) for the director distribution and Eqs. (35) and (36) to obtain the spectra in the frequency domain. First we consider the strong anchoring limit that occurs for samples $R \geq 0.3$ μm. These spectral patterns are not sensitive to the surface parameter σ since

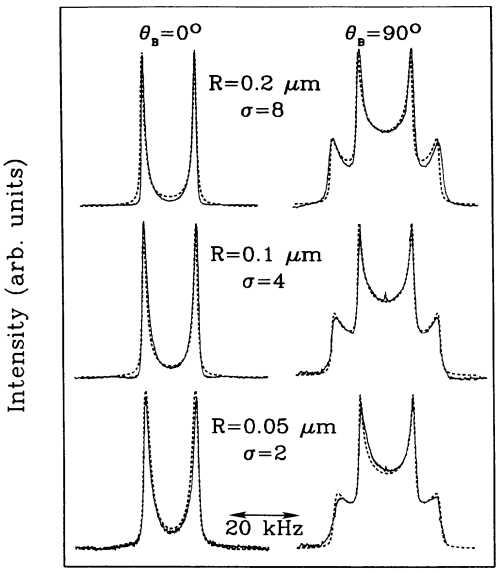

FIG. 15. Experimental ^{2}H-NMR spectral patterns (solid curve) of 5CB-βd_2 in Nuclepore membranes compared to theoretical simulations (dashed curve) for the ERPD structure varying the surface parameter σ to obtain the fit at constant defect density $L/R=1.5$. The spectra were recorded at 24 °C.

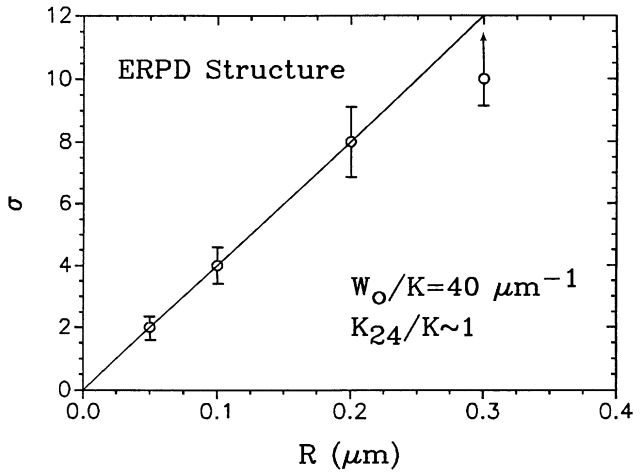

FIG. 16. The experimentally measured parameter σ as a function of cavity radii extracted from the ^{2}H-NMR spectral fits presented in Fig. 15.

the shape of the patterns can be fit for $\sigma \geq 10$. As the cylinder size is decreased, the intensity in the central region of the spectra increases for the $\theta_B=0°$ orientation as a consequence of weak anchoring. This is particularly noticeable for the $R=0.05$ μm sample. For the $\theta_B=90°$ orientation of the cylinder axis, the outer singularities decrease as the cylinder size is decreased due to the weakening of the effective anchoring strength at the surface driving a larger contribution of directors to escape along the cylinder axis. We were somewhat disappointed that the configuration did not undergo a transition, but calculations reveal that the ERPD structure is metastable and can remain locked in [25].

The best fits to the experimental spectra were obtained using values of $L/R=1.5$ and $\sigma=8$, 4, and 2 for cavity radii $R=0.2$, 0.1, and 0.05 μm. The molecular-anchoring strength W_0 and the surface elastic constant K_{24} can be uniquely determined by graphing $\sigma=RW_0/K+K_{24}/K-1$ as a function of R as shown in Fig. 16. This results in a linear relationship where W_0/K is the slope and the ordinate intercept yields the value of K_{24}/K. Using values of $K=5\times10^{-12}$ J/m, the molecular-anchoring strength is determined to be $W_0=2\times10^{-4}$ J/m^2 and $K_{24}=K$. Numerical solutions for the director distributions used in the simulations yield similar values of W_0 and K_{24} [37].

We applied a lecithin surfactant (Sigma Chemical Co.) to the cylinder walls to weaken the effective anchoring strength yet preserve the preferred perpendicular molecular orientation at the surface. The experimental ^{2}H-NMR spectra recorded at 24 °C are presented in Fig. 17 for three radii $R=0.3$, 0.4, and 0.5 μm. We were surprised to discover the existence of the PP configuration rather than the PR configuration for cavity radii $R \leq 0.4$ μm which led to the detailed theoretical treatment of this structure presented in Sec. II. This configuration yields two sharp singularities separated by $\frac{1}{2}\delta\nu_B$ with no further contributions for the $\theta_B=0°$ case. For the $\theta_B=90°$ case, the spectral pattern results in two singularities separated by $\delta\nu_B$ with a small contribution

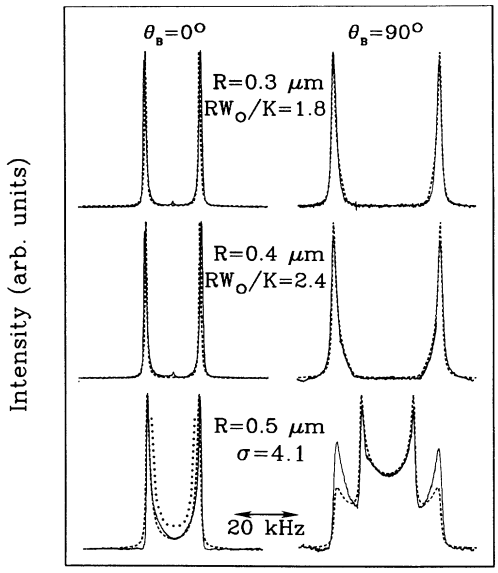

FIG. 17. Experimental ^{2}H-NMR spectral patterns (solid curve) of 5CB-βd_2 in Nuclepore membranes directly compared to theoretical simulations (dashed curve) for the ERPD structure $R=0.5$ μm ($L/R=1.5$) and PP structures $R \leq 0.4$ μm. The dotted curve for the $R=0.5$ μm sample represents the situation when $K_{24}/K=0$. The spectra were recorded at 24 °C.

in the center that depends on the cylinder size, i.e., the anchoring strength. This indicates that the symmetry axis of PP structure rotates to align parallel to the magnetic field in the presence of weak anchoring at the cavity wall. This sort of behavior also occurs in polymer dispersed liquid-crystal (PDLC) systems where the bipolar droplet will often align its symmetry axis parallel to the magnetic field [39]. The PP configuration transforms into the ERPD structure at $R \geq 0.5$ μm as can be seen from the spectrum in Fig. 17.

The PP$\rightarrow$ERPD transition proves to be particularly useful in determining the surface elastic constant K_{24} since it contributes to the ERPD structure and is absent in the description of the PP configuration. The value of RW_0/K is the only fitting parameter in the spectral simulation for the PP structure (dashed curve in Fig. 17) at the $\theta_B = 90°$ orientation. The $\theta_B = 0°$ orientation always yields two singularities at one-half the bulk quadrupole splitting frequency. The best fits were obtained using $RW_0/K = 1.8$ and 2.4 for cavities of radius 0.3 and 0.4 μm, respectively. Using a value of $K = 5 \times 10^{-12}$ J/m, the anchoring strength is calculated to be 3×10^{-5} J/m^2. Using this independent measurement of W_0 for the lecithin/5CB-βd_2 interface, it is then possible to extract K_{24}/K from the spectral fit for the ERPD structure that occurs at $R = 0.5$ μm. A good fit is obtained in the $\theta_B = 0°$ case which gives a value of $K_{24} = 1.1K$. The dotted curve in Fig. 17 for the $R = 0.5$ μm sample at the $\theta_B = 0°$ orientation is the corresponding spectrum assuming $K_{24}/K = 0$. The fit to the $\theta_B = 90°$ orientation is less satisfying at the $\theta = 0°$ singularities. We attribute this to the magnetic field strength that becomes a nuisance at larger cavity sizes where the cavity diameter approaches the magnetic coherence length and is further aggravated by the presence of weak anchoring at the cavity wall introduced by the lecithin treatment. This problem worsens for the next cavity size at $R = 1.0$ μm.

A crossover calculation that was presented in Sec. II provides a useful check on the magnitude of K_{24}/K. Since we do not have an exact solution to the free energy of the ERPD structure but only an approximate solution given by Eq. (31), we use the exact free energy for the ER structure given by Eq. (21) to estimate K_{24}/K based on the observation of the transition point. The calculation is made using the experimentally determined value of W_0 measured from the PP structure at the $\theta_B = 90°$ orientation of the cylinder axis and the observed value of $R_c = 0.5$ μm, where the nematic director-field transition takes place which yields a value of $K_{24}/K \sim 1.7$ as shown in Fig. 18. Adding defects to this calculation will increase this estimated value of K_{24}.

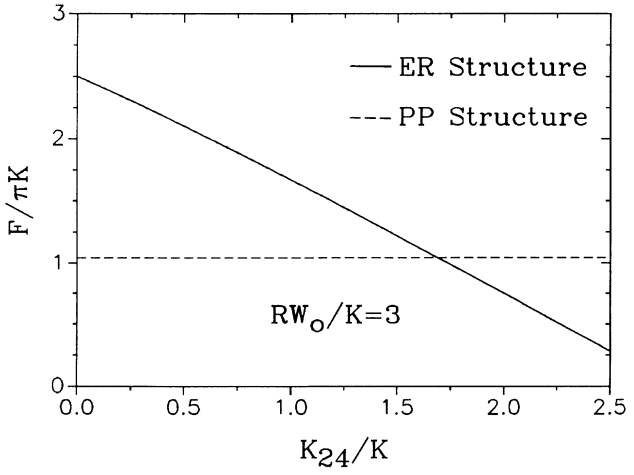

FIG. 18. Free energy per unit length as a function of K_{24}/K for the planar-polar (PP) and escaped-radial (ER) structures in the one-constant approximation calculated using the value of RW_0/K measured for the lecithin surface.

VI. CONCLUSIONS

It was demonstrated that the surface elastic term proportional to K_{24} plays an essential role in considering nematic structures subjected to weak molecular anchoring and high degrees of curvature. The cylindrical geometry and high density of pores exhibited by Nuclepore membranes allows nematic director-field configurations to be studied in submicrometer cavities where elastic energies become favorable to induce other kinds of configurations. The molecular-anchoring strength W_0 and surface elastic constant K_{24} must carefully be included into the theoretical treatment to describe the interesting physics that takes place when surface and elastic energies begin to compete in small cylinders. Untreated Nuclepore membranes when filled with 5CB-βd_2 provide an anchoring strength of sufficient magnitude to support the ERPD structure for $R \geq 0.05$ μm with a defect density $L/R \approx 1.5$, which is consistent with predictions [25]. Lecithin-modified Nuclepore surfaces are shown to weaken the anchoring strength by an order of magnitude only supporting this structure for $R \geq 0.5$ μm. At $R \leq 0.4$ μm the PP nematic configuration occurs rather than the PR structure. The sensitivity of the NMR technique to the nematic director distribution associated with the structure allows the detailed elastic properties such as K_{24} to be measured. The value of K_{24} is found to be comparable in magnitude to the bulk elastic constants.

We do not expect to observe the PR configuration predicted by Cladis and Kleman when the splay and bend elastic constants are similar and under normal anchoring conditions in view of the observed PP structure that is shown to be energetically favorable. However, one might expect the PR configuration to occur where there is unusually strong anchoring and in materials that exhibit a smectic phase where the bend deformation becomes expensive near the nematic-smectic transition [22,23,53].

The influence of the term proportional to K_{13} in the free energy, sometimes called the mixed-splay-bend term, is less obvious because it requires the inclusion of the volume elastic free-energy terms which have second derivatives in the director field. However, a rough estimate of its importance can be provided by considering the escaped-radial configuration in the one-constant approximation described by Eq. (18). The solution to the

Euler-Lagrange equation which neglected K_{13} can be substituted into $\int_{\text{vol}} K_{13}\text{div}(\mathbf{n}\,\text{div}\mathbf{n})dV$ to arrive at a first estimate on the contribution of the K_{13} term which results in the following expression:

$$F_{\text{ER}} \sim \pi K \left[3 - \frac{K_{24}}{K} - \frac{1}{\sigma} - \frac{8}{9}\frac{K_{13}}{K} \right] . \tag{37}$$

Again this estimate demonstrates that the K_{13} term contributes to the free energy if the surface elastic constant K_{13} is nonzero. The magnitude of K_{13} is unknown but its contribution to the nematic director field is expected to be less important than its K_{24} counterpart. The inclusion of K_{13} will force us to take into account the volume elastic free-energy terms which have second derivatives of the director field. This proves to be extremely involved and is a subject of future study.

ACKNOWLEDGMENTS

Research is supported in part by the National Science Foundation (NSF) under Solid State Chemistry Grant No. DMR88-176647 and Science and Technology Center ALCOM Grant No. DMR89-20147. The materials support was provided by Sandra Keast and resource facility of the NSF and National Center for Integrated Photon Technology (NCIPT) under DARPA Contract No. MDA 972-90-C-0037. Helpful discussions with Daniele Finotello are gratefully acknowledged.

[1] C. W. Oseen, Trans. Faraday Soc. **29**, 883 (1933).
[2] H. Zocher, Trans. Faraday Soc. **29**, 945 (1933).
[3] A. Scharkowski, A. Schmiedel, R. Stannarius and E. Weisshuhn, Z. Naturforsch. **45a**, 37 (1990).
[4] A. Beyer and U. Finkenzeller, *E. Merck Newsletter,* E. Merck, D-6100 Darmstadt, Frankfurter, Strasse 250, Germany.
[5] J. W. Doane, A. Golemme, J. L. West, J. B. Whitehead, Jr., B. G. Wu, Mol. Cryst. Liq. Cryst. **165**, 51 (1988).
[6] G. Srajer, F. Lonberg, and R. B. Meyer, Phys. Rev. Lett. **67**, 1102 (1991).
[7] O. D. Lavrentovich, Phys. Scr. **T39**, 394 (1991).
[8] J. H. Erdmann, S. Zumer, and J. W. Doane, Phys. Rev. Lett. **64**, 1907 (1990).
[9] S. Zumer, S. Kralj, and J. Bezic, Mol. Cryst. Liq. Cryst. **212**, 163 (1991).
[10] R. Ondris-Crawford, E. P. Boyko, B. G. Wagner, J. H. Erdmann, S. Zumer, and J. W. Doane, J. Appl. Phys. **69**, 1 (1991).
[11] S. Zumer (private communication).
[12] S. Kralj and S. Zumer, Phys. Rev. A **45**, 2461 (1992).
[13] E. Dzyaloshinskii, Zh. Eksp. Teor. Fiz. **31**, 773 (1970) [Sov. Phys.—JETP **33**, 773 (1970)].
[14] P. E. Cladis and M. Kleman, J. Phys. (Paris) **33**, 591 (1972).
[15] R. B. Meyer, Philos. Mag. **27**, 405 (1973).
[16] C. E. Williams, P. Pieranski, and P. E. Cladis, Phys. Rev. Lett. **29**, 90 (1972).
[17] C. Williams, P. E. Cladis, and M. Kleman, Mol. Cryst. Liq. Cryst. **21**, 355 (1973).
[18] P. G. de Gennes, *The Physics of Liquid Crystals* (Clarendon, Oxford, 1974).
[19] A. Saupe, Mol. Cryst. Liq. Cryst. **21**, 211 (1973).
[20] M. Kleman, *Points, Lines, and Walls in Liquid Crystals, Magnetic Systems, and Ordered Media* (Wiley, New York, 1988) and references therein.
[21] M. Kuzma and M. M. Labes, Mol. Cryst. Liq. Cryst. **100**, 103 (1983).
[22] P. E. Cladis, Philos. Mag. **29**, 641 (1974).
[23] P. E. Cladis, A. E. White, and W. F. Brinkman, J. Phys. (Paris) **40**, 325 (1979).
[24] G. P. Crawford, M. Vilfan, I. Vilfan, and J. W. Doane, Phys. Rev. A **43**, 835 (1991).
[25] I. Vilfan, M. Vilfan, and S. Zumer, Phys. Rev. A **43**, 6875 (1991).
[26] J. Nehring and A. Saupe, J. Chem. Phys. **54**, 337 (1971); **56**, 5527 (1972).
[27] G. Barbero and C. Oldano, Mol. Cryst. Liq. Cryst. **168**, 1 (1989); **170**, 99 (1989); A. Sparavigna, L. Komitov, and A. Strigazzi, Phys. Scr. **43**, 210 (1991).
[28] V. Hugo Schmidt, Phys. Rev. Lett. **64**, 535 (1990).
[29] D. W. Allender, G. P. Crawford, and J. W. Doane, Phys. Rev. Lett. **67**, 1442 (1991); G. P. Crawford, Ph. D. dissertation, Kent State University, 1991 (unpublished).
[30] J. Pirs, M. Olenik, B. Morin, S. Zumer, and J. W. Doane, J. Appl. Phys. **68**, 3826 (1991).
[31] Z. Yaniv, J. W. Doane, J. L. West, and W. Tamau-Lis, SID Jpn. Display XX, 572 (1990).
[32] J. W. Doane, in *Liquid Crystals: Applications and Uses,* edited by B. Bahadar (World Scientific, Teaneck, NJ, 1990), Chap. 14.
[33] A. Saupe, J. Chem. Phys. **75**, 5118 (1981).
[34] A. Rapini and M. Papoular, J. Phys. (Paris) Colloq. **30**, C4-54 (1969).
[35] M. Vilfan, V. Rutar, S. Zumer, G. Lahajnar, R. Blinc, J. W. Doane, and A. Golemme, J. Chem. Phys. **89**, 579 (1988).
[36] Ping Sheng, in *Introduction to Liquid Crystals,* edited by E. B. Priestley, P. J. Wojtowicz, and P. Sheng (Plenum, New York, 1975).
[37] G. P. Crawford, D. W. Allender, M. Vilfan, I. Vilfan, and J. W. Doane, Phys. Rev. A **44**, 2570 (1991).
[38] S. Hsia Chen and B. J. Liang, Appl. Phys. Lett. **59**, 1173 (1991).
[39] A. Golemme, S. Zumer, J. W. Doane, and M. Neubert, Phys. Rev. A **37**, 559 (1988).
[40] R. Stannarius, G. P. Crawford, L. C. Chien, and J. W. Doane, J. Appl. Phys. **70**, 1 (1991).
[41] A. Golemme, S. Zumer, D. W. Allender, and J. W. Doane, Phys. Rev. Lett. **61**, 1937 (1988).
[42] J. W. Doane, in *Magnetic Resonance of Phase Trnasitions,* edited by F. J. Owens, C. P. Poole, Jr., and H. A. Farach (Academic, New York, 1979), Chap. 4.
[43] G. P. Crawford, D. K. Yang, S. Zumer, D. Finotello, and J. W. Doane, Phys. Rev. Lett. **66**, 723 (1991).
[44] G. P. Crawford, R. Stannarius and J. W. Doane, Phys.

Rev. A **44**, 2558 (1991).
[45] A. Abragam, *The Principles of Nuclear Magnetism* (Oxford University Press, London, 1961).
[46] G. Chidichimo, Z. Yaniv, N. P. Vaz, and J. W. Doane, Phys. Rev. A **25**, 25 (1982).
[47] Nuclepore Corporation, 7035 Commerce Circle, Pleasanton, CA 94566.
[48] J. C. Moore, *The Development of a New Membrane Filter* (American Laboratory, New York, 1969).
[49] Sandra Keast and Mary Neubert (private communication).
[50] M. C. Porter, A *Novel Membrane Filter for the Laboratory* (American Laboratory, New York, 1974).
[51] F. M. Gasparini, G. Agnolet, and J. D. Reppy, Phys. Rev. B **29**, 138 (1984).
[52] Daniale Finotello (private communication).
[53] H. Hakemi, Liq. Cryst. **5**, 334 (1989).

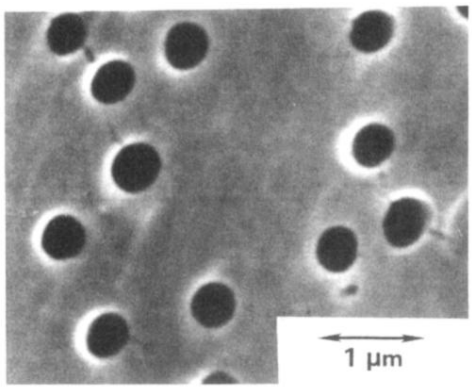

FIG. 14. Scanning electron microscope (SEM) photograph of a Nuclepore membrane with pores of radius 0.4 μm.

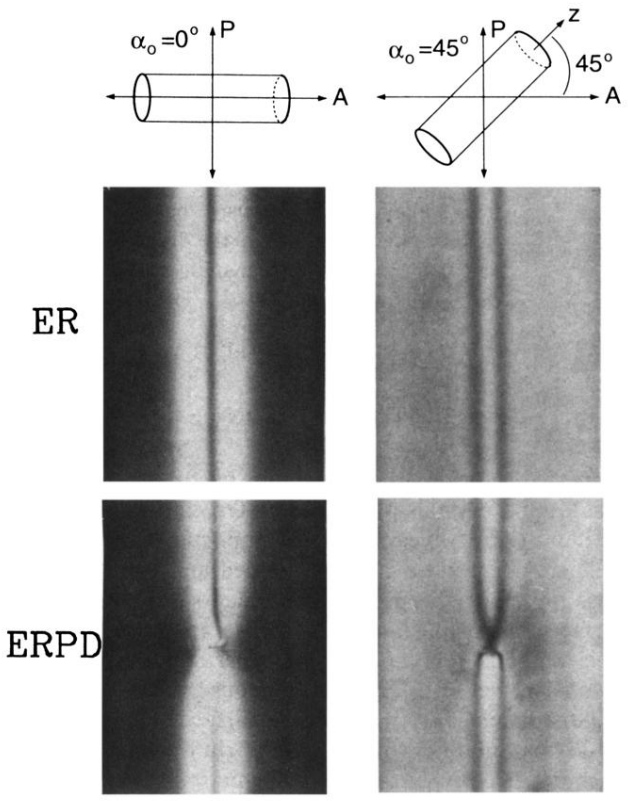

FIG. 2. Optical birefringence patterns of the escaped-radial configuration using a while-light source. The sample is prepared by filling a 200-μm-diam capillary tube treated with lecithin with the liquid-crystal compound 4′-pentyl-4-cyanobiphenyl (5CB). The continuous escaped-radial structure (a) and the escaped-radial structure with a defect (b) is presented for two orientations of the cylindrical axis with respect to the initial polarization vector (α_0=0° and 45°). For a more detailed discussion of optical microscopy studies on capillary tubes consult Refs. [15–23].